EPJ AP
Applied Physics
EPJ.org
your physics journal

Eur. Phys. J. Appl. Phys. (2013) 63: 30901 DOI: 10.1051/epjap/2013120522

Design of an axial flux PM motor using magnetic and thermal equivalent network

Romain-Bernard Mignot, Raynal Glises, Christophe Espanet, Emeline Saint Ellier, Frédéric Dubas, and Didier Chamagne

edp sciences

The title "The European Physical Journal" is a joint property of EDP Sciences, Società Italiana di Fisica (SIF) and Springer

Eur. Phys. J. Appl. Phys. (2013) 63: 30901
DOI: 10.1051/epjap/2013120522

THE EUROPEAN PHYSICAL JOURNAL
APPLIED PHYSICS

Regular Article

Design of an axial flux PM motor using magnetic and thermal equivalent network

Romain-Bernard Mignot, Raynal Glises[a], Christophe Espanet, Emeline Saint Ellier, Frédéric Dubas, and Didier Chamagne

Department ENERGY, UMR 6174 CNRS, FEMTO-ST Institute, 90010 Belfort, France

Received: 28 November 2012 / Received in final form: 1 April 2013 / Accepted: 15 July 2013
Published online: 3 September 2013 –

Abstract. This paper deals with the development of a new generation of electric motors (7.5–15 kW) for automotive powertrains. The target is a full electric direct drive vehicle, for the particular application to heavy quadricycles. An original axial flux PM structure is proposed due to the simplicity of its manufacturing. However it leads to a 3D structure, difficult to study. The paper deals with analytical models that can be used to achieve the analysis and the sizing of the motor. The electromagnetic behavior is modeled using a simple magnetic equivalent network and the thermal behavior is analyzed with a thermal network. Finally, the analytical results are compared to those experimentally obtained and it proves the interest of the proposed structure: the construction is simple and the performances are satisfying.

1 Introduction

The industrial development of all-electric vehicles or hybrid electric vehicles needs the development of efficient, reliable and low cost electrical drives. In this context, the authors have studied an original axial flux PM structure. The interest of this structure lies in a simple manufacturing, but the drawback is that the 3D structure is a complex one. In the first developments of the motor design, there is thus a need of analytical models in order to achieve the sizing of the motor and, possibly, its optimization. In this context, this paper presents analytical models to study the electromagnetic and thermal behavior of the proposed motor.

The electrical, magnetic and thermal phenomena are tightly coupled together in electrical machines. The temperature distribution is the consequence of the power losses distribution, which depends on the temperature of the electric and magnetic material properties. Moreover, the proposed permanent magnet machine has a complex 3D mechanical structure and, consequently, relatively complex ways of thermal losses. However, the temperature prediction is mandatory, because there are different temperature limits for the used materials, such as insulations and magnets. The calculation of losses is then necessary in a first approach and later a thermal model can be coupled to the electromagnetic model to predict correctly the temperature distribution in the machine. A number of studies have investigated the temperature distribution in rotating machines. For example, Sahin suggested a lumped parameter thermal equivalent circuit to study the thermal effect of a quarter model of a single sided axial-flux permanent magnet machine in her dissertation [1]. Cannistra and Labini analyzed the temperature distribution of a three-phase squirrel-cage deep-bars asynchronous motor by using finite element method [2]. Separated rotor and stator thermal networks were used in the study. The two networks were determined by the network boundary conditions (ambient temperatures). In a series of papers [3,4] by Staton et al., the thermal characteristics of electric motors were investigated by using a commercially available software package called Motor-CAD. Computational fluid dynamics and lumped circuit analysis were used in the optimization of the motor thermal design. Bousbaine et al. developed a three-dimensional (circumferential, axial and radial) model for a single-phase permanent-split-capacitor induction motor by coupling the three independent networks [5].

In this paper, the authors present first the axial flux PM machine and the specifications linked to the particular applications to heavy quadricycles motorizations (see Tab. 1). The choice of the electric machine structure is also justified. Then, in a second part, the authors detail the magnetic equivalent circuit (MEC) they have developed to analyze the magnetic behavior of the machine. In addition, electric parameters are calculated in order to determine the motor losses. In a third part, the authors detail the thermal network that has been suggested to predict the thermal behavior, knowing the thermal losses. Both electromagnetic and thermal models results are compared with the ones obtained with experimental tests.

[a] e-mail: raynal.glises@univ-fcomte.fr

Table 1. Technical characteristics.

V_{vehicle} : 90 km h	Wheel/tire: 135/70-R15	Battery voltage: 350 V
γ : 0 at 50 km h in 13 s	C_x: 0.35	m_{vehicle}: 850 kg
Slope at 50 km h: 11%	S_{frontal}: 1, 8 m^2	K_{bearing}: 0.01

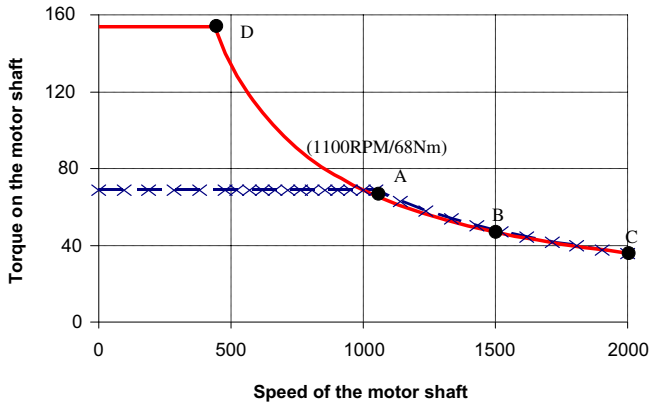

Fig. 1. Boundary characteristics of torque/speed of the motorization.

2 Prototype: constraints and description

2.1 Specifications

In this paragraph, the authors present the calculation of the motor specifications according to those of the electric vehicle, in which the machine should be installed. The maximal speed of the vehicle equals 110 km h^{-1}, we consider a direct drive. One electrical machine is coupled to each front wheel. The technical characteristics of the electric vehicle are then given in Table 1. Later, using the mechanical laws, it is possible to obtain the torque/speed characteristic of the motorization shown in Figure 1.

2.2 Motorization choice and presentation of the axial flux permanent magnet machines (AFPMM)

The first step of the design deals with the right choice of the motor type. In this paper, it has been chosen to focus only on the axial flux permanent magnet machines since those machines are of high interest in terms of torque and power densities. In this context, in 2004, Aydin et al. [6] have identified several structures. Unfortunately, these structures do not really match with the following specifications dealing with a low cost machine:

- a stator with the smallest possible quantity of iron,
- stator windings using pre-wired coils,
- a light rotor with reduced quantity of iron.

Hosseini et al. [7] and Jung et al. [8] have presented the same original structure, which can meet our specifications. Hosseini et al. [7] have developed a generator prototype of 500 W for a voltage of 40 V. It is a radial flux generator with a stator shaped in "U" and a concentrated winding. There are 12 "U" for 24 magnets. The rotor is made of circular permanents magnets. Jung et al. [8] have developed a motor to obtain 60 Nm for 550 rpm. It is a radial flux motor with a stator shaped in "U" and a concentrated winding. There are 12 "U" for 16 magnets. Each stator is composed of simple U-shaped magnetic circuits and the rotor is made of composite material including circular permanent magnets. It is clear that the quantity of iron used in the stator and the rotor is quite reduced. In addition, the coils can be pre-wired before assembling the motor. Coles et al. [9] and Parviainen et al. [10] have used winding techniques similar to those used in this article.

Our final choice is therefore focused on a physical structure including some of the ideas developed in these two papers. In addition we have proposed the following points to improve its layout:

- a thickened rotor to make it more rigid and stable when loaded,
- the use of stator studs on one arm of the "U", which has the advantage to:
  (i) limit the connection lengths between each coil of one phase, and
  (ii) to obtain a strengthened rotor and to remove the magnetic leakage between internal and external rotor permanent magnets.

The stator and the rotor are respectively shown in Figures 2 and 3. The objective is to propose a design enabling gains in terms of production cost and in terms of

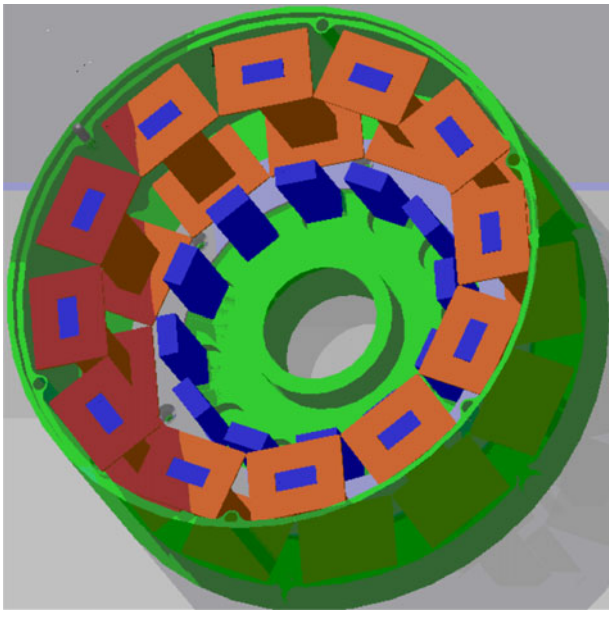

Fig. 2. Half stator yoke.

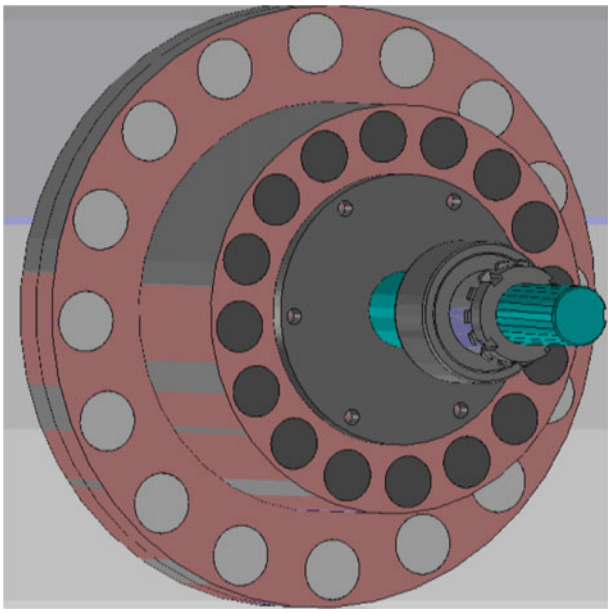

Fig. 3. Rotor in composite structure with magnetic bar and circular PMs.

construction process. Thus, all the motor parts are simple and can be quickly realized.

The stator is made of two identical mechanical parts, composed of 12 independent U-shape magnetic circuits. On each magnetic circuit an insulating casing, which supports the different coils, is mounted. One phase consists in eight coils evenly distributed.

The rotor is made of 16 circular PMs. The flow of magnetic flux between the PMs on both sides of the rotor is possible thanks to the insertion of laminated magnetic bars as shown in Figure 3. The laminated magnetic bars offer the same quality as the stators shaped in "U", which is M330–35. The size of each laminated magnetic bar is identical in one "U". The rotor is manufactured from a two-parts injecting mold. The insertion of the bars is made in one of the two parts of rotor. The two parts of the rotor are fixed together.

3 Electromagnetic modeling of the axial flux permanent magnet machines

Due to the fact that the magnetic flux (in particular the flux leakages) is fundamentally 3D, the design and optimization steps of an AFPMM would require a 3D calculation. The easiest way is probably to use a 3D FEM modeling. Nevertheless, this method is not sufficiently explicit in comparison with analytical modeling (i.e., reluctances networks [11] or symbolic resolution of Maxwell's equations with or without slots). Indeed, with sufficient assumptions, the magnetic field can be commonly expressed in the form of analytical solutions, which makes the model more flexible and more suitable for pre-design, for parametric analysis or for optimization. Then, we propose to use a simple magnetic equivalent circuit (MEC), which is presented in this paragraph. Indeed, the stator geometry of the motorization and the flux are purely axial and not multi-transverse. Indeed, the average flux line through the surface S of each stator circuit is two-dimensional (X and Z axes). Therefore, we can apply the Ampere Law in 2D, the magnetic field being considered purely radial in the air-gap. The magnetic leakages in the air gap are not taken into account. So we can apply the law of flux conservation. Even if the geometry is 3D, this simplification makes the representation of the electromagnetic phenomena sufficient in 2D. In the next paragraphs, the analytical results of the AM are compared to experimental tests in order to analyze its relevance and its interest, in an industrial context.

3.1 Modeling assumptions and description of the magnetic equivalent circuit

To achieve the modeling, we assume that the MEC is static and, in a first approach, that the flux distribution is 2D. With such a MEC, it is possible to calculate various parameters, such as fluxes, back electromotive forces, electromagnetic torque, magnetic losses and demagnetization.

Figure 4 represents an axial cross-section of one phase 2D magnetic circuit. The effects of the magnetic saturation, inter-PM and inter-coil leakage, and the PMs losses are neglected.

3.2 The parameters of the stator circuit

3.2.1 Magnetic characteristics of the PM at Ta = 20 °C [12]

The technical characteristics of the used PM (i.e., type: UHT 38UH) are shown in Table 2. This choice is explained

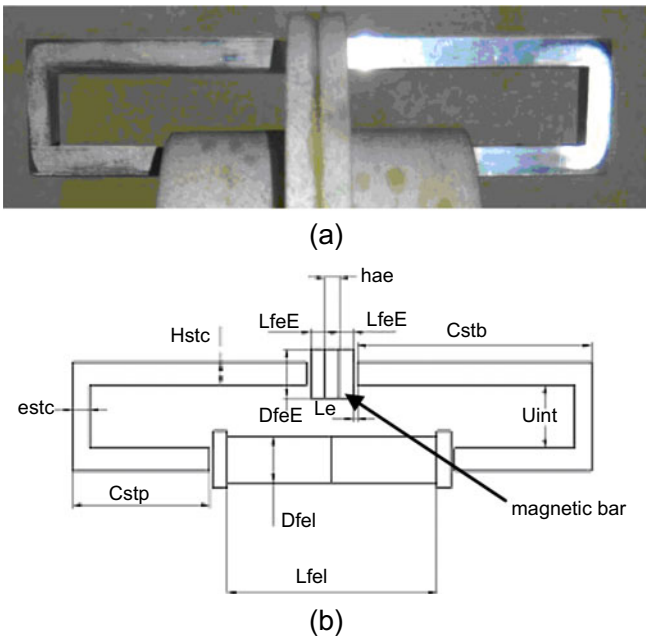

Fig. 4. Magnetic circuit of a phase: (a) picture, (b) axial section.

Table 2. Technical characteristics of the PM.

UHT 38UH		
Bra_20: 1,26T	Hcb: 963 kA/m	Hcj: −1990 kA/m
$\mu_{ra} : 1,05$	$\alpha_B : -0,001$	$\alpha_H : -0,005$

by the high probability of having a high temperature due to the stator windings, this high temperature being at the origin of demagnetization problems following extended rated working. The remanent flux density of the PMs depends on the temperature as following:

$$B_{ra}(T_a) = B_{ra\_20^\circ}\left[1 + \alpha_B(T_a - 20)\right] \quad [T], \tag{1}$$

where T_a is the ambient operating temperature and α_B the temperature coefficient of the material.

Regarding the demagnetization, the magnetic field limit of the PM is defined by:

$$H_{90\%}(T_a) = H_{90\%\_20^\circ}\left[1 + \alpha_H(T_a - 20)\right] \quad [A\,m^{-1}], \tag{2}$$

where α_H represents the temperature coefficient of the magnetic field.

3.2.2 Air-gap flux density [13]

The air-gap flux density is expressed applying the Ampere Law and the flux conservation:

$$H_a(T_a) = \frac{-B_{ra}(T_a)}{\mu_0\mu_{ra}\left(1 + \frac{h_{ae}S_e}{\mu_{ra}L_eS_a}\right)} \quad [A\,m^{-1}], \tag{3}$$

where μ_{ra} represents the relative magnetic permeability of the PMs, S_a the surface of the PMs, S_e the surface of the air-gap, h_{ae} the thickness of the PMs and L_e the width of the air-gap.

Knowing the $H_a(T_a)$ characteristics and a given value of the air-gap (L_e), the PMs thickness (h_{ae}) is calculated in order to reach the specified torque. Thus, it is possible to evaluate the PM flux density, $B_a(T_a)$, and the air-gap one, $B_e(T_a)$:

$$B_a(T_a) = \mu_0\mu_{ra}H_a(T_a) + B_{ra}(T_a) \quad [T], \tag{4a}$$

$$B_e(T_a) = B_a(T_a)\frac{S_a}{S_e} \quad [T]. \tag{4b}$$

Regarding the materials cost (in particular the PM cost), it is interesting to minimize the PMs volume. A classical solution is to maximize the energy stored in the air-gap which is deduced from the theoretical maximum energy stored in the PM during the motor working. The air-gap energy is maximal for a flux density equal to $B_{a\_Evershed}(T_a) = B_{ra}(T_a)/2$. This value enables to define the minimum thickness of the PM h_{ae_min} required to satisfy the Evershed criteria (maximization of the air-gap energy).

The PM magnetic energy is defined by [14]:

$$W_{evershed/magnet}(T_a) = B_a(T_a)H_a(T_a) \quad [J]. \tag{5}$$

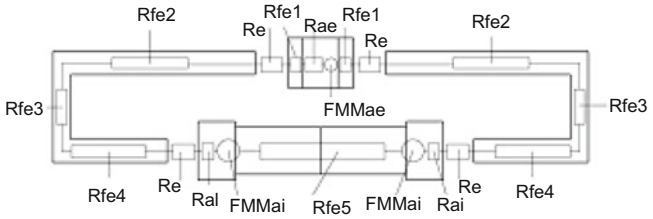

Fig. 5. Representation of the reluctances networks.

Then, the minimum PM thickness is given by:

$$h_{ae\_min}(T_a) = -\frac{B_{a\_Evershed}(T_a)L_eS_a}{H_a(T_a)\mu_0S_e} \quad [mm]. \tag{6}$$

This value of the PM thickness, $h_{ae} = h_{ae\_min}$, causes iterative recalculation of all the magnetic circuit parameters.

3.2.3 Minimum PM thickness to avoid demagnetization [15]

The minimum volume to support the demagnetizing field imposed by the stator currents of the windings is h_{ae_demag}. As the circular section of the rotor magnets cannot structurally exceed a given size, we need to adjust its thickness h_{ae_min}.

Neglecting magnetic leakage and consumption of Ampere-turns in ferromagnetic parts, the minimum PM thickness is deduced from the armature reaction field:

$$h_{ae\_demag}(T_a) = \mu_{ra}S_a\left[\frac{\mu_0 2N_sI_{eff}}{S_eB_e(T_a)} + \frac{L_e}{S_e}\right] \quad [mm], \tag{7}$$

$$h_{ae\_min}(T_a) \geq h_{ae\_demag}(T_a) \quad [mm], \tag{8}$$

where N_s represents the number of coils and I_{eff} the RMS current in a stator phase. Once again, this new value for the PM thickness $h_{ae} = h_{ae\_min}$ causes iterative recalculation of all the magnetic circuit parameters.

3.2.4 Magnetic flux and flux density in the magnetic circuit

The magnetic flux, as well as the flux density in each magnetic circuit part, depends on the value of the PMs magnetomotive force, $F_{mm}(T_a)$, and of the overall reluctance of the circuit R_c. The representation of the magnetic network is shown in Figure 5.

The MMF magnitude of the PMs is given by:

$$F_{mm}(T_a) = \frac{B_a(T_a)h_{ae\_min}}{\mu_{ra}\mu_0} \quad [A], \tag{9}$$

and the overall reluctance of the circuit by:

$$R_c = 2\left(R_{fe1} + R_{fe2} + R_{fe3} + R_{fe4} + 2R_e + R_{aI}\right) + R_{ae} + R_{fe5} \quad [H^{-1}], \tag{10}$$

where R_i represents the index value of the reluctances of each part of the magnetic circuit (which means two

ferromagnetic circuits shaped in "U", the 3 PMs and the two air-gaps).

The magnetic flux magnitude flowing in the magnetic circuit is defined by:

$$\phi_{\mathrm{c}}(T_{\mathrm{a}}) = F_{\mathrm{mm}}(T_{\mathrm{a}})/R_{\mathrm{c}} \quad [\mathrm{Wb}]. \tag{11}$$

The magnetic flux density magnitude in each magnetic circuit part is calculated using the conservation flux.

3.3 Electrical parameters of the AM

3.3.1 Electrical resistance of one phase

The resistance of a winding is classically expressed with:

$$R_{\mathrm{ph}}(Tc) = \frac{\rho_{\mathrm{cu}}(T_{\mathrm{c}})L_{\mathrm{winding}}}{S_{\mathrm{winding}}} \quad [\Omega], \tag{12}$$

where L_{winding} is the winding length of one phase, $\rho_{\mathrm{cu}}(T_{\mathrm{b}})$ the copper resistivity and S_{winding} the conductors cross-section.

3.3.2 Self-inductance of a-one phase

The inductance of each phase depends on the number of turns and on the reluctance of the magnetic circuit. The self-inductance of one phase is thus defined by:

$$L_{\mathrm{p_{ph}}} = \frac{N_{\mathrm{s}}^2}{R_{\mathrm{c}}} N_{\mathrm{c_{ph}}} \quad [\mathrm{H}], \tag{13}$$

where $N_{\mathrm{c_{ph}}}$ is the number of magnetic circuits of one phase.

3.3.3 Single-phase model

The motorization is star-connected and powered by a PWM voltage inverter. The maximal RMS voltage of one phase is thus expressed by:

$$V_{\mathrm{ph/N}} = \sqrt{2}\frac{U_{\mathrm{dc}}}{\pi} \quad [\mathrm{V}], \tag{14}$$

where U_{dc} is the DC voltage of the inverter.

The RMS back EMF is given by:

$$E_{\mathrm{ph/N}}(T_{\mathrm{a}}) = \frac{2\pi}{\sqrt{2}} \left(N_{\mathrm{s}} N_{\mathrm{c_{ph}}}\right) f_{\mathrm{s}} \Phi_{\mathrm{c}}(T_{\mathrm{a}}) \quad [\mathrm{V}], \tag{15}$$

where f_{s} is the stator electrical frequency.

The back EMF coefficient is defined by:

$$K_{\mathrm{fem_{ph/N}}}(T_{\mathrm{a}}) = \frac{E_{\mathrm{ph/N}}(T_{\mathrm{a}})}{\Omega_{\mathrm{s}}} \quad [\mathrm{V\ s\ rad^{-1}}], \tag{16}$$

where Ω_{s} is the rotor mechanical angular velocity.

Table 3. Technical characteristics of the ferromagnetic sheets.

$M330$–35			
P_f: 3, 3 W	Mass: 1 kg	f: 50 Hz	B_{const}: 1, 5 T

The RMS current of one phase is expressed by:

$$I_{\mathrm{eff}} = \frac{T_{\mathrm{em}}}{3K_{\mathrm{fem_{ph/N}}}(T_{\mathrm{a}})} \quad [\mathrm{A}], \tag{17}$$

where T_{em} is the electromagnetic torque, which is considered equal to the effective torque required by the specifications. The effect of the armature reaction is neglected.

The equivalent single-phase model assumes that the rotor has non-salient pole. Indeed, the PMs are mounted on a mechanical structure, which has a relative magnetic permeability very close to the one of the vacuum. Then the equivalent single-phase model is given by:

$$\underline{V}_{\mathrm{ph/N}} = \underline{E}_{\mathrm{ph/N}}(T_{\mathrm{a}}) + R_{\mathrm{ph}}(T_{\mathrm{b}})\underline{I}_{\mathrm{eff}} + jLp_{\mathrm{ph}}\omega_{\mathrm{s}}\underline{I}_{\mathrm{eff}} \quad [\mathrm{V}], \tag{18}$$

where ω_{s} is the electrical pulsation in rad s^{-1}.

3.3.4 Losses of the AFPMM [16,17]

The AFPMM losses deal with copper losses and iron losses. The copper losses are expressed by:

$$P_j(T_{\mathrm{c}}) = 3R_{\mathrm{ph}}(T_{\mathrm{c}})\underline{I}_{\mathrm{eff}}^2 \quad [\mathrm{W}]. \tag{19}$$

And, the iron losses are calculated with:

$$P_{\mathrm{Iron}} = (K_{\mathrm{Fouc}}\omega_{\mathrm{s}} + K_{\mathrm{Hyst}})\omega_{\mathrm{s}} B_{\mathrm{Iron}}^2 m_{\mathrm{Iron}} \quad [\mathrm{W}], \tag{20}$$

where $K_{\mathrm{Fouc}} \sim K_{\mathrm{hyst}}$ are the coefficients of iron losses, B_{Iron} the flux density magnitude, and m_{Iron} the laminations mass. The magnetic characteristics of the used laminations are provided by the manufacturer and are given in Table 3.

The Foucault and hysteresis coefficients are respectively given by:

$$K_{\mathrm{fouc}} = \frac{e_{\mathrm{Iron}}^2}{24\upsilon_{\mathrm{Iron}}\rho_{\mathrm{Iron}}} \quad [\mathrm{A^2\ m^2\ s^3\ kg^{-2}}], \tag{21a}$$

$$K_{\mathrm{hyst}} = \frac{P_{\mathrm{f}} - \left(K_{\mathrm{Fouc}}\omega_{\mathrm{const}}^2 B_{\mathrm{const}}^2\right)}{\omega_{\mathrm{const}} B_{\mathrm{const}}^2} \quad [\mathrm{A^2\ m^2\ s^2\ kg^{-2}}], \tag{21b}$$

where e_{Iron} is the thickness of the laminations, υ_{Iron} the flux density magnitude, ω_{const} the electrical pulsation, and $\rho_{\mathrm{Iron}}$the electrical resistivity of the laminations.

3.3.5 Electromagnetic power and efficiency

The electromagnetic power is expressed by:

$$P_{\mathrm{em}} = 3\,K_{\mathrm{torque}}(T_{\mathrm{a}})I_{\mathrm{eff}}\omega_{\mathrm{s}} \quad [\mathrm{W}], \tag{22}$$

Table 4. Results of the AFPMM magnetic parameters.

$B_a(T_a)$	0.85T	$F_{mm}(T_a)$	9800 A
$B(T_a)$	1.6T	R_c	65.5×10^6 H^{-1}
h_{ae_min}	12.5 mm	$\Phi_c(T_a)$	150×10^{-6} Wb

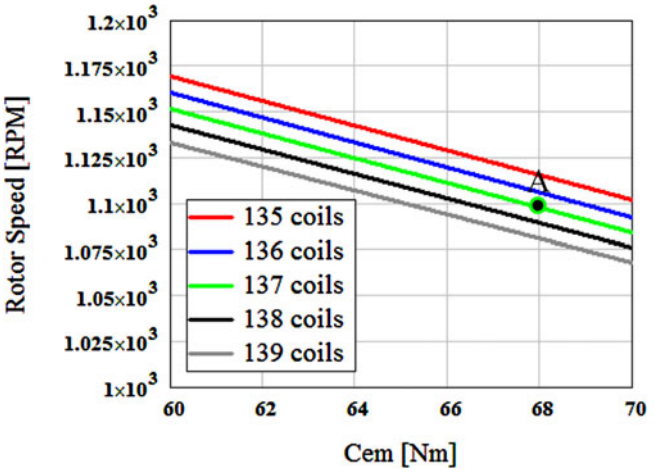

Fig. 6. Nrotor = f (Cem) according to the number of coils for a phase.

where K_{torque} is the torque coefficient, which is equal to $K_{fem_{ph/N}}$.

Finally, the efficiency of the AFPMM is then given by:

$$\eta(T_a, T_c) = \frac{P_{em}(T_a)}{P_{em}(T_a) + Pj(T_c) + P_{fer}} \quad [\%]. \qquad (23)$$

3.4 Calculation of the number of turns

The maximum external size of the motor is imposed by the specifications, and for a given minimum volume of the rotor and air-gap (purely mechanical reasons), it is possible to determine the geometric variables of the 12 stator magnetic circuits. The magnetic characteristics of the resulting motor are then calculated for $T_a = T_b$ given by the thermal equivalent circuit presented further. The results are presented in Table 4.

The electromagnetic torque is given in Figure 1 (point A). The results are shown in Figure 6 and we have obtained 137 turns per coil, i.e., 1096 turns for one complete phase.

Table 5 summarizes the characteristics of the designed machine according to the torque imposed by the mechanical load and for the different operating points shown in Figure 1.

3.5 Comparison between computed and experimental results

3.5.1 Test bench description

Figure 7 shows the AFPMM with each coil available in order to change the winding connections. A torquemeter enables to measure the torque as shown in Figure 8.

Table 5. Results of the electrical parameters of the AFPMM.

1096 Coils	T_{em} (Nm)	N (RPM)	Id (A)	Iq (A)	η (%)
Point A	68	1100	0	23	90.4
Point B	47	1523	−8.5	17,3	93.1
Point C	35.8	2000	−16	14	92.4
Point D	151	476	0	54	71.2

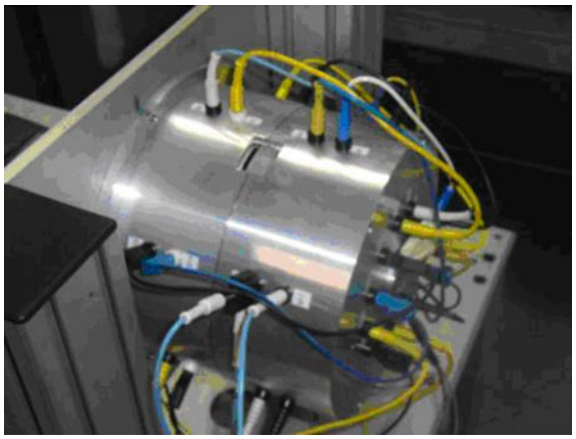

Fig. 7. The AFPMM.

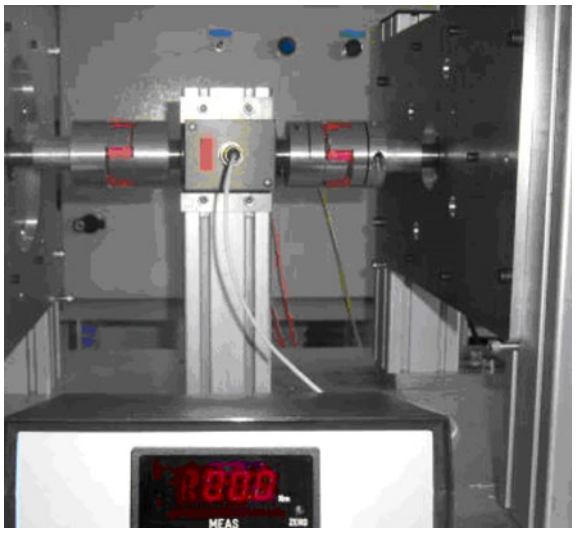

Fig. 8. Dynamic torque meter.

3.5.2 Comparison between theoretical and experimental results

The measurement was performed for the entire speed range, without flux weakening, from 0 to 1100 tr/min. For the point A, the results are represented in Table 6. The experimental working point at 1100 rpm has been verified by measuring the rotating speed with an external optical tachometer (and controlling the frequency given by a sinus/cosinus encoder). The base speed equals to 1000 rpm. The base speed equals to 1000 rpm. This rotating speed has been measured using (1) the signals given by the sin/cos position sensor and (2) the VSI which gives the information on the speed too. Indeed, this speed corresponds to the saturation mode of the VSI.

Table 6. Comparison between calculated and experimental results.

Point A	T_{em} (Nm)	N (rpm)	E (V)	Iq (A)	R (Ω)	L (mH)	η (%)
MEC (1)	68	1100	109	23	0.5	3.6	90.4
Experimental test (2)	68	1000	86	26.8	0.5	4.74	86.5
[(2)–(1)]/(2)	0%	−10%	−26%	14.2%	0%	24%	−4.5%

The power factor equals to 0.69 at base speed. The low value of the power factor is due to the high inductance and the relatively low air-gap flux density for this first prototype. However, it is clear that it leads to an oversizing of the VSI (current of the switches). Thus, the optimization of the machine regarding the construction cost is due to an increase of the VSI price.

The electromagnetic equations developed in the article are based on the Behn-Eschenburg's model, which is only used for a motorization without saliency and without saturation. This choice enables to quickly obtain the RMS back EMF values and the cyclic self-inductance. This information is essential to know the electromagnetic performances of the machine.

The differences between practical and theoretical results show the limits of this simple modeling. It appears that there is an effect of rotor saliency. The latter imposes a different value of the stator inductance in the d and q axes. Moreover, the experimental value of the RMS back EMF peak shows that there are leakages between magnets in the rotor.

A new dynamic modeling by magnetic equivalent circuit, taking into account leakages in the rotor and magnetic saturation, should bring an improvement of the motor electromagnetic performances evaluation. But, on the other hand, this model gives a sufficient modeling of the losses for the thermal model that is detailed in the next paragraphs.

4 Transient thermal modeling of the motor with a nodal thermal network

4.1 Introduction

The nodal thermal network used for the thermal modeling of the motor is particularly efficient because it can represent very easily 2D and 3D structures [2,18], for transient or steady state thermal modeling. Moreover, it has the benefit to be easily computed and solved compared to the 2D and 3D finite elements modeling [19,20]. Moreover, compared to this latter method, the thermal modeling by nodal network permits easily to apply local boundary conditions for all the different type of machines (permanent magnets, synchronous or asynchronous) [1,21].

A 3D nodal network has been chosen in our study and this for many reasons. Indeed, the particularity of 2D thermal modeling is that the heat fluxes in the third axis are never considered. In that way, heat losses that are not considered in this third direction bring eventually to an overestimation of the simulated temperatures compared to the real ones. On the opposite, a 2D modeling avoids considering a heat power source in the volume, when the third dimension is considered, eventually giving an underestimation of the simulated temperatures compared to real ones. In that way, only a 3D modeling enables to make the simulated results very close to the real temperatures, as it can be seen in the following parts of this paper. We have finally chosen a nodal network for our study. Indeed, this method by nodal network allows very easily to modify the nodal discretization of the studied structure by only modifying the matrix of the mathematical model (see Sect. 4.2, Eqs. 24 and 25) containing the geometrical parameters of the motor, without changing its topology. The methods by FE are not so flexible because the meshed structures are relatively fixed. Furthermore, the chosen method enables to apply more easily local boundary conditions like heat flows (convection and/or radiation) or surface temperatures. Finally, in the future, this method will be extended with the association (strong mathematical coupling) of the existing model with the fluidic model (turbulent or laminar). Indeed, such coupled resolution is at the moment very hard to carry out using the FE method. The discretization and the resolution of the transient thermal model of the structure have been made thanks to the mathematical software MATHCAD. That method has been developed for a simplified 3D structure of the studied motor. Nevertheless, symmetry plans for boundary conditions, internal generated heat power and naturally geometry have enabled to strongly simplify the structure of the motor into the basic representation given in Figure 9, showing respectively axial and radial views of the modeled machine.

They are linked through the heat transfers in the windings of the stator which are located in the region of most important heat generation in the machine. Moreover, the high value of the thermal conductivities of the winding in this axis justifies the link of the two plans in that area (i.e., a 3D model). Compared to these axial heat fluxes, other heat transfers in the third dimension of the iron and of the yoke can be neglected without penalizing the quality and the validity of the computation results.

4.2 Nodal thermal network, equivalence with an electrical network

With these analogies, it is also possible to take into account conduction, convection and radiation phenomena [22,23]. Moreover, but it has not been discussed in our study; the mass transfer can also be taken into account. The phenomena of radiation in the IR range

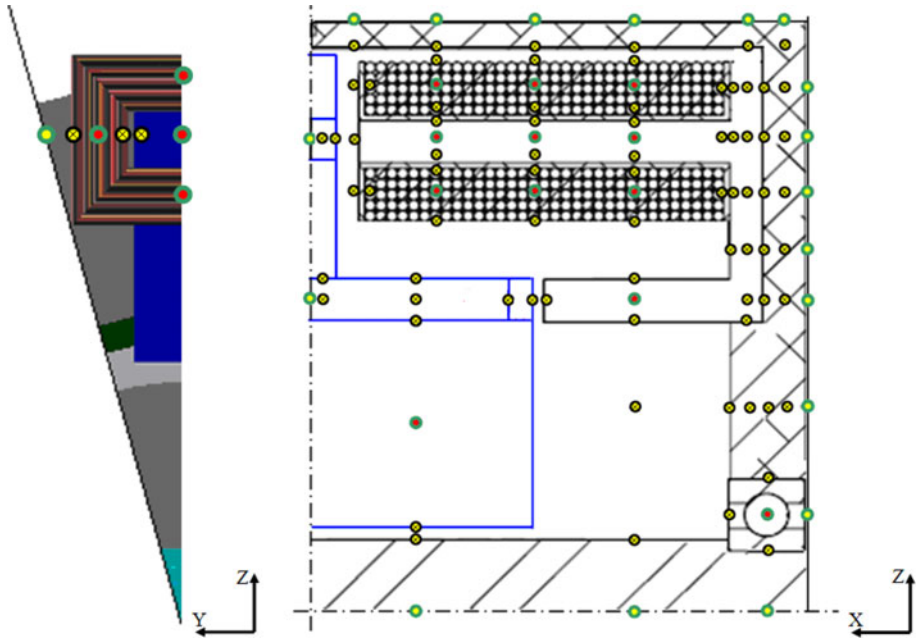

Fig. 9. Radial and axial views of the modeled structure with the thermal nodes.

have normally been neglected considering the relatively low level of temperature of the external surfaces.

The main methodology consists of the achievement of the energy balance between two different blocks in contact, blocks which are assumed to be isothermal volumes. This energy balance is done between two nodes located at the center of these isothermal blocks. The initial studied structure is also subdivided into several isothermal blocks defined as the thermal network. Figure 10 gives as example a representation of a 2D-block exchanging energy (and eventually mass) with four surrounding isothermal elements. Nevertheless, the representation of a 3D structure could be very easily represented with six surrounding elements. Thermal conductances are homogeneous to the inverse ratio of the thermal resistance. Its dimension is W m^{-1} K^{-1} as for a thermal conductivity.

Table 7 gives the different expressions of these thermal conductances in the case of conduction, convection and radiation phenomena and for the particular case of thermal fluxes obtained by a transfer of mass.

From a general point of view, the completion of the thermal modeling of the studied structure consists of making the heat energy balance for each isothermal element. Finally, there is the same number of algebraic equations as nodes. The general expression (case of the thermal transient state) of the heat energy balance can be expressed by the equation (24) given by:

$$C_i \frac{\mathrm{d}T_i}{\mathrm{d}t} = \sum_j G_{ij}^{\mathrm{cond}}(T_j - T_i) + \sum_k G_{\mathrm{ik}}^{\mathrm{rad}}(T_k - T_i) + \sum_k G_{\mathrm{il}}^{\mathrm{conv}}(T_l - T_i) + H_i(t) \quad [\mathrm{W}]. \qquad (24)$$

where G^{cond}, G^{conv} and G^{rad} respectively represent the thermal conductances (W m^{-1} K^{-1}) by conduction, convection and radiation between two neighbored nodes. $H_i(t)$ is the internal heat power generation function of the time (W m^{-3}) at the node i.

It is also necessary to transform these algebraic equations into a tensor system as following, in equation (25):

$$\begin{bmatrix} G_{1,1} & G_{1,2} \rightarrow & G_{1,n} \\ G_{2,1} & G_{2,2} \rightarrow & G_{2,n} \\ \downarrow & \downarrow \rightarrow & \downarrow \\ G_{n,1} & G_{n,2} \rightarrow & G_{n,n} \end{bmatrix} \begin{bmatrix} T_1 \\ T_2 \\ \downarrow \\ T_{n-1} \\ T_n \end{bmatrix} + \begin{bmatrix} H_1 \\ H_2 \\ \downarrow \\ H_{n-1} \\ H_n \end{bmatrix} = \begin{bmatrix} C_1 & 0 \rightarrow & 0 & 0 \\ 0 & C_2 \rightarrow & 0 & 0 \\ 0 & 0 \rightarrow & 0 & 0 \\ 0 & 0 \rightarrow & C_{n-1} & 0 \\ 0 & 0 \rightarrow & 0 & C_n \end{bmatrix} \begin{bmatrix} \frac{\partial T1}{\partial t} \\ \frac{\partial T2}{\partial t} \\ \downarrow \\ \frac{\partial Tn-1}{\partial t} \\ \frac{\partial Tn}{\partial t} \end{bmatrix} [W]. \qquad (25)$$

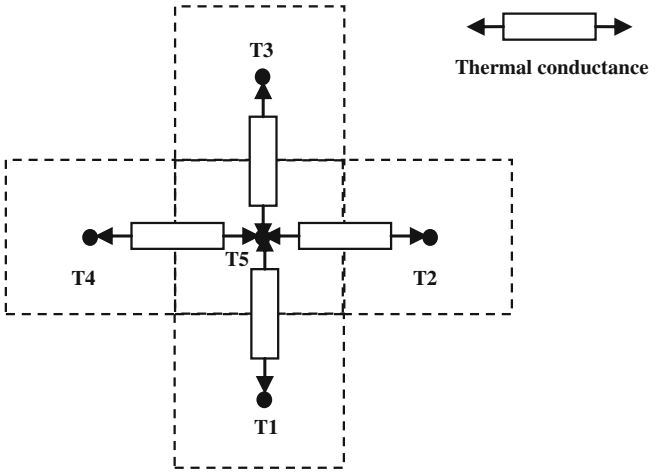

Fig. 10. Representation of a 2D isothermal element with surrounding elements.

Table 7. Expressions of thermal conductances and thermal fluxes.

Heat transfer	Expression of the flux	Expression of the conductance
Conduction	$\frac{\lambda S_{ij}}{L_{ij}}(T_j - T_i)$[1]	$G_{ij}^{\text{cond}} = \frac{\lambda S_{ij}}{L_{ij}}$
Convection	$h\ S(T_\text{s} - T_i)$	$G_{\text{is}}^{\text{conv}} = hS$
Radiation for black body	$\sigma S_i F_{ij}(T_j^4 - T_i^4)$	$G_{ij}^{\text{rad}} = \sigma S_i F_{ij}(T_j^2 + T_i^2)(T_i + T_j)$
Fluid flow	$\dot{m}\, c(T_j - T_i)$[2]	$G_{ij}^{f} = \dot{m}\, c$

[1] S_{ij} surface of transfer between volumes (i) and (j), L_{ij} length between the nodes i and j
[2] $\dot{m}$ mass flow (kg s^{-1})

This matrix system of equation (25) can be easily solved thanks a RK2 (RK: Range-Kutta) or RK4 method. In the case of a thermal transient state thermal study, the system (25) is also transformed into the equation (26) which can be easily solved through a direct method.

$$\begin{bmatrix} G_{1,1} & G_{1,2} \to G_{1,n} \\ G_{2,1} & G_{2,2} \to G_{2,n} \\ \downarrow & \downarrow \to \downarrow \\ G_{n,1} & G_{n,2} \to G_{n,n} \end{bmatrix} \begin{bmatrix} T_1 \\ T_2 \\ \downarrow \\ T_{n-1} \\ T_n \end{bmatrix} + \begin{bmatrix} H_1 \\ H_2 \\ \downarrow \\ H_{n-1} \\ H_n \end{bmatrix} = 0 \quad [W]. \tag{26}$$

4.3 Boundary conditions and thermophysical properties of the material

4.3.1 Coefficient by convection at the internal and external air-solids interfaces [22,23]

The best solution regarding these particular parameters should be to consider a local value. Unfortunately, as always in such problems, it is hard to get it because of the high difficulty to obtain all the local temperatures. Moreover it is impossible without disrupting the local heat fluxes. We thus considered a spatial average value of this parameter both on the internal and external surfaces of the machine. The convection is considered as free on the external surface and forced inside.

Determination of the external convection coefficient
Classically, the dimensionless number Grashof Gr is at first determined to estimate the nature of the flow around the carter. For that, we have considered the average external temperature of the surface T_s at 180 °C given by a pyrometer during the experimental test. The external temperature T_amb is 20 °C.

$$Gr = \frac{\beta g\, |T_\text{s} - T_\text{amb}|\, D_\text{h}^3}{\nu^2} \quad [-], \tag{27}$$

with β the coefficient of compressibility of the air (K^{-1}), g the gravitational acceleration (m s^{-2}), D_h the hydraulic diameter (m) and ν the kinetic viscosity (m^2 s^{-1}).

Finally, the value of Gr is 84×10^6. With the Prandtl's number Pr estimated to 0.686 it can be shown that the air flow around the motor is lightly turbulent. The expression of the Nusselt's number Nu is then the classical one, so that:

$$Nu = 0.135\,(GrPr)^{1/3} \quad [-], \tag{28}$$

Its value is 51.8.

Lastly, the value of the convection coefficient is given by the following and classical expression of the Nu which is representative of the heat transfer by convection at the interface compared to the transfer by conduction in the fluid.

$$h = Nu \times \lambda / D_h \quad [\text{W m}^{-2}\ \text{K}^{-1}], \tag{29}$$

where λ is the thermal conductivity of the air at the average temperature of the surface and the external air. We obtained $h = 9.7$ W m^{-2} K^{-1}.

Determination of the internal convection coefficient
The convection is, in this area, considered as forced because of the rotation speed of the rotor. The speed of the air at the interface is also given by the linear speed of the rotor. For a rotation speed $\omega = 1100$ rpm and a diameter of the rotor D_h of 50 mm, the maximum speed of the air to consider inside is 11.5 m s^{-1}.

Considering the internal surface of the stator as the surface of a duct which internal diameter is the characteristic length, the dimensionless Reynolds number Re which compares the inertia forces to the viscosity forces is also given by the expression:

$$Re = V D_\text{h} / \nu \quad [-]. \tag{30}$$

Its value is 71128.

This value of the Reynolds number indicates that the flow is fully turbulent. Lastly, the expression of the internal heat convection coefficient as function of the Nusselt's number Nu can be given by the classical expression:

$$h = \frac{\lambda}{D_\text{h}} Nu = 0.023 \frac{\lambda}{D_\text{h}} \left(1 + \frac{D_\text{h}}{L}\right)^{0.7} \times Re^{0.8} Pr^{0.4} \quad [\text{W m}^{-2}\,\text{K}^{-1}], \tag{31}$$

with L the length of the internal surface of the stator. The value of the internal convection coefficient is $h =$ 35 W m^{-2} K^{-1}.

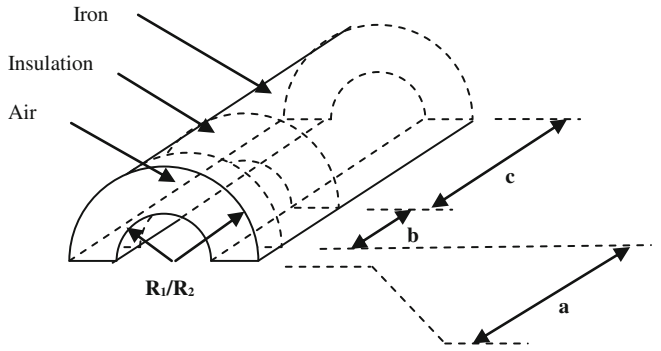

Fig. 11. Simplistic representation of the sheet steels of the machine (not at scale).

4.3.2 Determination of the matrix of conductivities of the iron and the windings

Determination of the conductivities of the iron sheets

The iron can be considered as an inhomogeneous volume that transfers the heat fluxes along the axis of the machine with a high difficulty. In that way, because of the geometry, the equivalent conductivity along the radius tends to the value of the iron whereas its value along the axis of the machine takes a very low value.

The sheets are an association of air, insulation and iron. These elements are placed in series along the axis of the machine. Thus the global thermal resistance equals the sum of the thermal resistance of these elements taken separately. Along the radius of the machine, these elements are placed in parallel. Therefore the inverse of the global thermal resistance is equal to the sum of the inverse of the thermal resistance of the considered elements. These associations can be shown in Figure 11.

The expression of the equivalent thermal conductivities, respectively expressed according the axis and the radius of the machine, are:

see equation (32) *below.*

The final kept values of the equivalent thermal conductivities for the sheets of iron along the axis and the radius of the machine are respectively 5 and 50 W m^{-1} K^{-1}.

Determination of the equivalent thermal conductivities of the wires of copper along the axis and the radius of the machine

The same way as for the iron sheets, the bundle of wires of the machine is an inhomogeneous area which presents different thermal characteristics along the axis and the radius of the machine. Its determination along the axis is very easy because the air, the insulations and the wires can be considered as a summation of parallel structures as shown in Figure 12a.

Finally, the conductivity along axis can be analytically determined [24,25]. The expression is:

$$\lambda_{\text{equivalent,axis}} = \lambda_{\text{copper}}\tau + \lambda_{\text{Insulation}}\beta + \lambda_{\text{Air}}(1-\tau-\beta) \quad [\text{W m}^{-1}\,\text{K}^{-1}], \tag{33-a}$$

with:

$$\tau = \frac{S_{\text{coper}}}{S}; \beta = \frac{S_{\text{Insulation}}}{S}; S_{\text{Air}} = (1-\tau-\beta)S, \tag{33-b}$$

where S is the total cross-section of the bundle of conductor. Finally the value of $\lambda_{\text{Equivalent,axis}}$ is 250 W m^{-1} K^{-1}. That relatively high value comes from the low thermal resistance of the winding along the axis of the wire (axis O, Z in Fig. 12a). In this geometry, the copper of the wire with the very high thermal conductivity constitutes a thermal bridge allowing the heat losses in this dimension.

On the other hand, the determination of the equivalent thermal conductivity along the radius is more complex and only a numerical simulation by EF enables to calculate it [24,26]. It is necessary to consider a minimal structure (see Fig. 12b) of the radial part of the bundle of conductors. Hence, the basic structure of the wires (Fig. 13) is computed (thermal steady state) in order to determine the final radial equivalent conductivity.

To be able to use the Fourier's law in our computation, it is necessary to vertically force the heat flux along the axis O, y, consequently to isolate the vertical surfaces. The expression of the equivalent thermal conductivity along the vertical axis O, y (according to Fig. 13) is given thanks the classical Fourier's equation by:

$$\lambda_{\text{equivalent,Y}} = \frac{a\phi_{\text{y}}}{(bc)(T_{\text{av,calculated}} - T_0)}. \tag{34}$$

In this expression, ϕ_{y} is the flux applied on the surface bc, T_0 is the imposed Dirichlet temperature on the horizontal surface at the opposite surface where the heat flux is applied. These two parameters can be chosen freely. Indeed, no matter the reached simulated temperatures, only the coefficient of the radial thermal conductivity eventually obtained is the goal. And whatever are the chosen parameters, the calculated radial conductivity is always the same, for a given geometry. Finally, the computation with the EF software gives easily the average value $T_{\text{av,calculated}}$ where the heat flux is applied. Then, it is also easy to calculate the equivalent thermal conductivity

$$\begin{cases} \lambda_{\text{equivalent,axis}} = (a+b+c)\left[\frac{a}{\lambda_{\text{Air}}} + \frac{b}{\lambda_{\text{Insulation}}} + \frac{c}{\lambda_{\text{Iron}}}\right]^{-1} \\ \lambda_{\text{equivalent,radius}} = \frac{1}{(a+b+c)}\left[a\lambda_{\text{Air}} + b\lambda_{\text{Insulation}} + c\lambda_{\text{Iron}}\right] \end{cases} \quad [\text{W m}^{-1}\,\text{K}^{-1}] \tag{32}$$

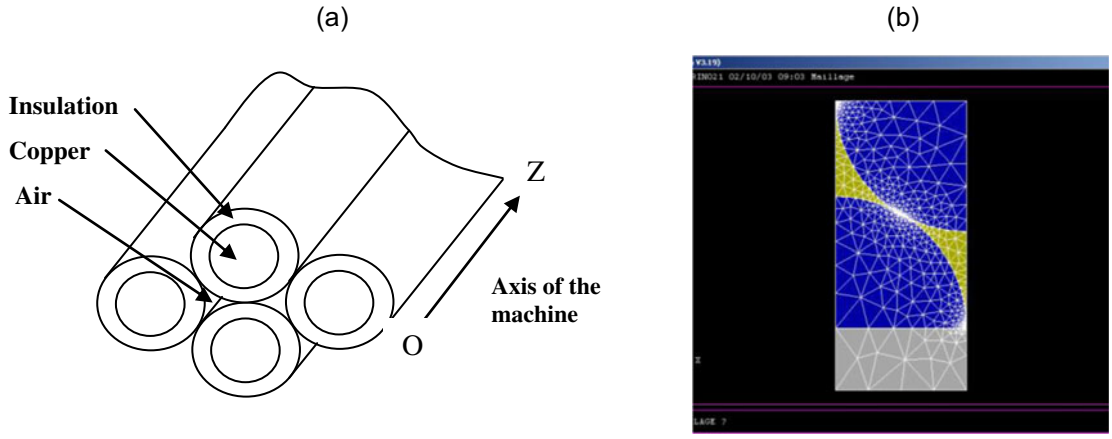

Fig. 12. Structure of the wires – minimum computed structure (plan x, y).

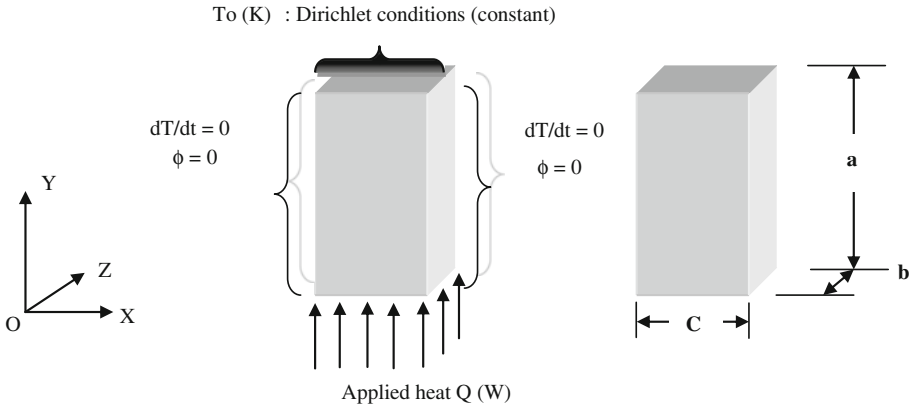

Fig. 13. 2D thermal computation of the basic radial element of the bundle of wire [26].

along the axis O, y. It is about 0.9 W m^{-1} K^{-1}, whatever are the applied heat flux or the Dirichlet temperature T_0, considering a maximum compactness of the electrical wires.

In a similar way, the thermal conductivity along the axis O, x can be easily determined. Nevertheless, the same value as the one obtained along the axis O, y is considered, knowing that the arrangement of the wires is with a high compactness.

Compared to the axial thermal conductivity, the obtained value is very small because of the absence of thermal bridge in the direction O, x and O, y. In that way, the insulation capabilities of the air and the insulation material are determining on the final result.

4.4 Validation of the computation

4.4.1 Introduction

As usually admitted, it is strongly necessary to join experimental results to numerical computations to validate the developed software. Indeed, only the experimental tests allow determining and localizing different internal heat generation. Moreover, only these lasts experimentations enable to apply the well adapted boundary conditions on the external surface.

Besides, the measurement of external and internal temperatures during experimental tests allowed the comparison of computed and experimental temperatures at the same points of the geometry. Finally, comparison and convergence of these temperatures according to a defined criterion allows considering the model as valid.

Moreover, the best way to obtain an operational computation tool should consist of making two different kinds of tests, for example at different loads. After having validated the two different tests, it is also possible to exploit the software by interpolating results, internal sources and boundary conditions between these two extreme points of functioning.

4.4.2 Computed and experimental tests. Implantation of the thermocouples

Only one initial experimental test has been realized for a nominal load of 70 N m. For this test, the feeding current is 25 A. The stator of the motor has been equipped with four thermocouples located in particular and sensible areas of the structure: the center of the windings (thermocouple 1), on the inside surface of the cylindrical carter (thermocouple 2), on the inside axial plan surface of the

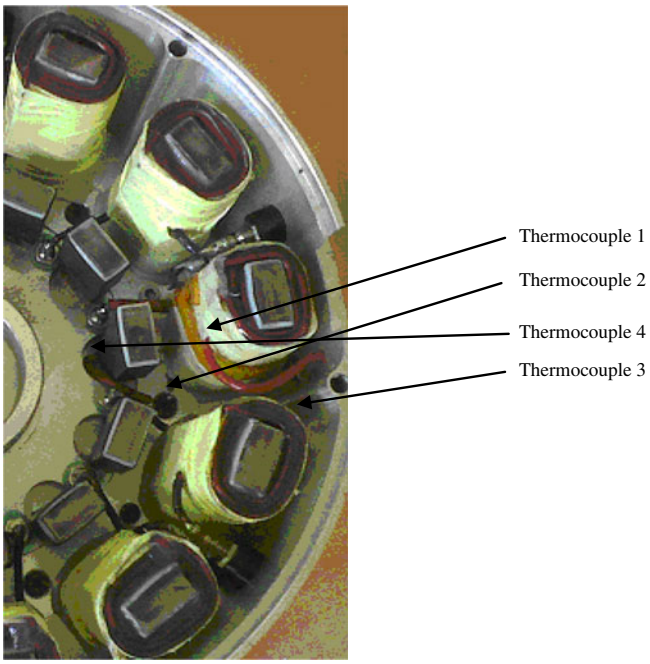

Fig. 14. Location of the internal thermocouples.

carter (thermocouple 3) and at last on the surface of the ferromagnetic circuit (thermocouple 4).

The photography on Figure 14 shows the location of these thermocouples. They are K type-thermocouples, which were elaborated, tested and calibrated (comparison with a PT 100 sensor) in our laboratory. Their diameter is 100 μm with a precision of 0, 3 K. The time of response is considered as immediate by comparison with the thermal inertia of the studied motor.

4.4.3 Comparison of the experimental and computed results: validation of the computation tool

All the relative differences in the following analysis are given as the expression:

$$\mathrm{DR} = \frac{T_{\mathrm{exp}} - T_{\mathrm{computed}}}{T_{\mathrm{exp}}} \quad [\%]. \tag{35}$$

Only two figures of experimental and computed results are here presented and compared during the thermal steady and transient states for two locations of the sensors. To limit the figures, we have chosen the ferromagnetic circuit and the windings because of their sensibilities with temperature.

It can be seen on Figure 15a, which represents the temperature as function on the time on the windings a good convergence between experimental and computed results. Indeed, the difference does not exceed -15% during the transient state (at time of 400 s). Nevertheless, this difference is due to a misunderstanding of the density value, which is very difficult to estimate as well, and especially as the thermal capacity of this inhomogeneous structure. As it can be seen, the difference for the steady state is unimportant being close to 0%. The appearance of the steady state can be estimated at the time $t = 2200$ s.

For the comparison of the experimental and computed results of temperature on the ferromagnetic circuit (see Fig. 15b), the same analysis as the one made for the windings can be developed with a maximum difference of 20% during the transient state at the time $t = 266$ s. However, a small difference of 3% on the temperatures can be observed for the steady state that is supposed to appear at the time $t = 1300$ s.

Table 8 summarizes the results for the two lasts locations of the thermocouples close to the yoke and compares them with the computed results.

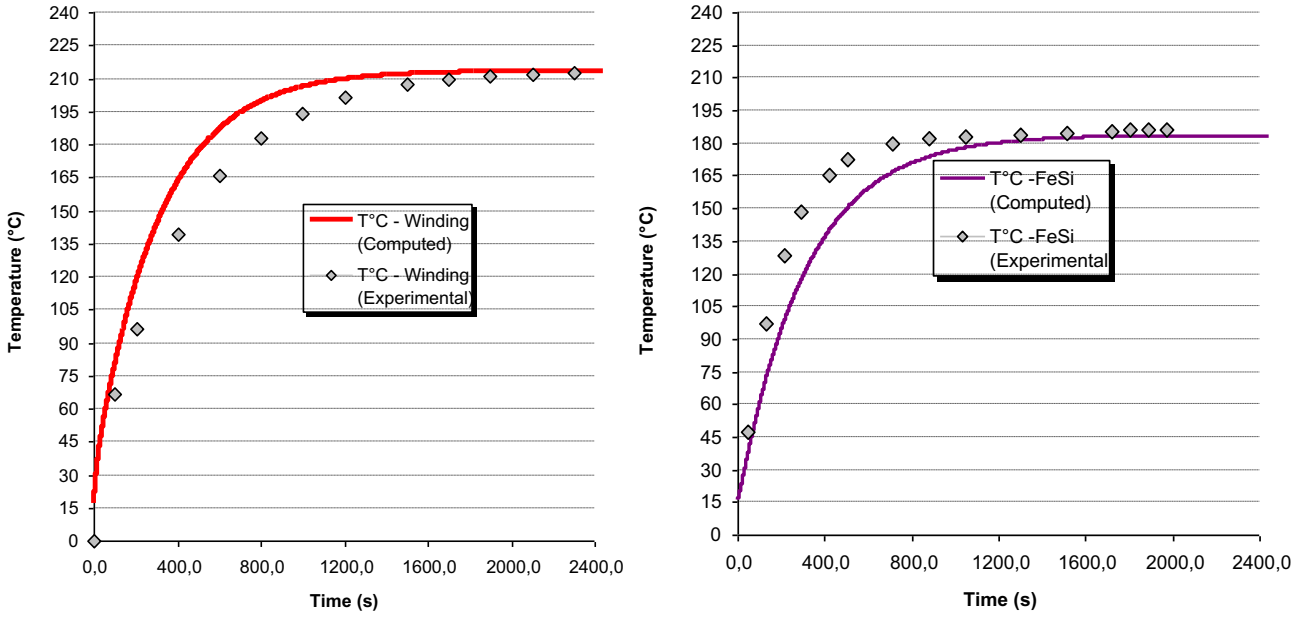

Fig. 15. Comparison of the experimental and computed temperatures in the windings and on the ferromagnetic circuit.

Table 8. Summary of the experimental and computed temperatures at the location of thermocouples No. 3 and No. 4

Thermocouple	Thermal transient state		Thermal steady state	
	DR_{max}	At time (s)	DR_{max}	Time of appearance of the steady state (s)
No. 3	19%	280	−5%	1300
No. 4	21%	300	9%	1500

Considering the relatively good quality of our presented results, we can consider the model as validated at this operating point and in restricted ranges on the torque, the intensity and the ambient temperature values.

5 Conclusion and outlooks for the magnetic and thermal equivalent models

In this paper, we have proposed the electrical, magnetic and thermal modeling of an original axial flux PM motor, using magnetic, electric and thermal equivalent circuits, the electromagnetic model feeding the thermal one. The results are satisfying and the models are valuable in the context of pre-design in an industrial context. But several improvements could be of a high interest, especially to provide higher accuracy.

Firstly, considering the magnetic results, the improvements should include the evaluation of the flux leakages between the PMs that are placed on the same radius of the rotor, to take into account the magnetic circuit saturation and the flux concentration in the magnetic bars that creates a saliency effect. With such improvements, the self-inductance, the mutual-inductance and the no-load PM flux could be calculated more precisely, without enlarging too much the calculation time.

Secondly, considering the thermal computation, the way of improvement should be:

- to make the extension of the 3D computation to the iron and not only to the windings,
- to obtain more accurate values of thermophysical values as the heat capacities for different sensible structures of the motor and especially for the inhomogeneous areas (windings, iron),
- to calculate local coefficient of convection at the interfaces between air and surfaces of the motor, so internal as external.

And the last but not the least, other constraining working points have to be analyzed in order to extend the forecast operating range of the machine. However these further studies will eventually lead to a more complex computed model. It will as usually be one limit of such developments.

In a close future, for the thermal transient model, it is considered to take into account the fluidic and conduction models for all the parts of the motor. The mathematical model based on the nodal network will also consider all the thermal transfer modes so that the mass transfer in the internal structure of the machine. This strongly non-linear system should also be simultaneously solved enabling to reach more accurate final temperatures. Then, a far perspective on which we begin to work will consist in the implementation of the coupled magnetic and heat and mass transfer models based on the same network, in the worst case, separately solved, at best, simultaneously solved.

The work presented in this paper has been achieved in the framework of the TRAX project, which is carried by a consortium of industrial companies (Nief-Plastic, R. Bourgeois, Schneider-Electric, Peugeot-Jappy, Phenix-International) and laboratories of the university and the CNRS (Departement ENERGY of the FEMTO-ST Institute – Scientific National Research Center and INSA-Lyon). This project has been selected by the French FUI (Interministerial Funds) and the French cluster "Véhicule Du Futur" and will be co-funded by the regional fund of innovation and the French Government.

The goal of the project is to develop a new generation of more effective and economic motors for the electric and hybrid vehicles. These machines will have a power range from 7.5 to 15 kW, which will enable to propose successful solutions in terms of specific power and energy efficiency for these new vehicles.

References

1. S. Funda, Ph.D. thesis, Technical University of Eindhoven, 2001
2. G. Cannistra, M.S. Labini, in *Proceedings of Electrical Machines and Drives* (IET, 1991), pp. 300–304
3. D.A. Staton, E. So, in *Proceedings of Industry Applications*, vol. 1 (IEEE, 1998), pp. 1–49
4. D. Staton, A. Boglietti, A. Cavagnino, in *Proceedings of Electric Machines and Drives*, vol. 2 (IEEE, 2003), pp. 747–755
5. A. Bousbaine, M. McCormick, W.F. Low, in *Proceedings of Electrical Machines and Drives* (IET, 1997), pp. 175–179
6. M. Aydin, S. Huang, T.A. Lipo, in *Proceedings of Symposium on Power Electronics, Electrical Drives, Automation, and Motion (SPEEDAM), 2004*
7. S. Hosseini, J. Shokrollahi Moghani, N. Farrokhzad Ershad, B. Bech Jensen, IEEE Trans. Magn. **47**, 772 (2011)
8. Y.-B. Jung, T. Long, J. Nelson, C. Landon, in *Proceedings of EET-2008 European Ele-Drive Conference and International Advanced Mobility Forum, 2008*
9. P.C. Coles, D. Rodger, R.J. Hill-Cottingham, H.C. Lai, M. Lamperth, A. Walker, in *Proceedings of Power Electronics, Machines and Drives*, vol. 2 (IET, 2004), pp. 840–843
10. A. Parviainen, J. Pyrhonen, P. Kontkanen, in *Proceedings of Electric Machines and Drives* (IEEE, 2005), pp. 1187–1191

11. R. Madhavan, B.G. Fernandes, in *Proceedings of International Conference on Electrical Machines 19th* (IEEE, 2010), pp. 1–6
12. `www.tdk.co.com`
13. H.C. Lowatt, P.A. Watterson, IEEE Trans. Magn. **35**, 505 (1999)
14. `www.lmats.com`, "Magnetic Test Methods" pdf, 2008
15. B. Multon, "Application of magnets to electrical machines", médiathèque ENSC, 2006.
16. P. Madina, J. Poza, G. Ugalde, G. Almandoz, in *Proceedings of Power Electronics and Applications* (IEEE, 2011), pp. 1–9
17. `www.rbourgeois.com`
18. N. Rostami, M. Feyzi, J. Pyrhonen, A. Parviainen, M. Niemela, IEEE Trans. Magn. **49**, 1178 (2012)
19. R. Glises, A. Miraoui, J.-M. Kauffmann, Thermal modelling for an induction motor, J. Phys. III France **3**, 1849 (1993)
20. R. Glises, D. Chamagne, J.-M. Kauffmann, in *Proceedings of International Conference on Electrical Machines 15th* (Emerald Group Publishing Limited, 2002)
21. J. Kaye, S.W. Gouse, IEEE Trans. Power Appar. Syst. **75**, 1468 (1957)
22. M.N. Ozisik, *Heat Transfer: A Basic Approach* (McGraw-Hill Inc., 1985)
23. W.M. Rohsenow, J.P. Hartnett, *Handbook of Heat Transfer* (McGraw-Hill Inc., 1973)
24. E. Matagne, in *Proceedings of International Symposium on Modelling and Simulation of Electrical Machines, and Static Converters* (IEEE, Nancy, 1990), pp. 189–193
25. G.S. Springer, S.W. Tsai, J. Compos. Mater. **1**, 166 (1967)
26. R. Glises, R. Bernard, D. Chamagne, J.-M. Kauffmann, J. Phys. III France **6**, 1389 (1996)